Report

Cell Reports

Origin of Gamma Frequency Power during Hippocampal Sharp-Wave Ripples

Graphical Abstract

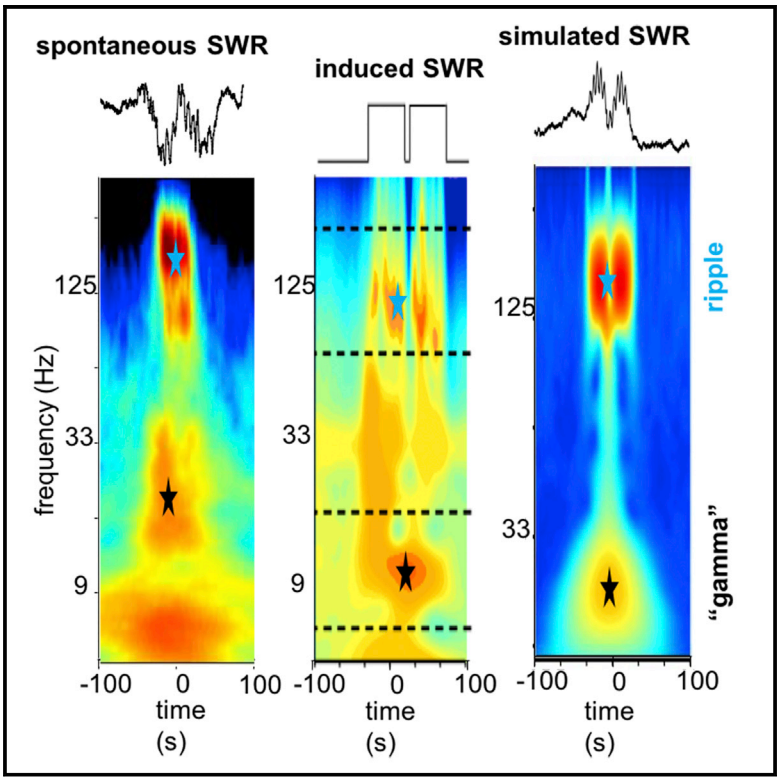

Authors

Azahara Oliva, Antonio Fernández-Ruiz, Eliezyer Fermino de Oliveira, György Buzsáki

Correspondence

gyorgy.buzsaki@nyumc.org

In Brief

SWRs are thought to support memory consolidation and planning. They are characterized by several spectral components: a slow-frequency wave (sharp-wave), a high-frequency oscillation (ripple), and a slow "gamma" band. Here, we report a mechanism, involving the concatenation of several SWRs, which explains the generation of the "gamma" frequency band.

Highlights

- Gamma power arises due to concatenated sharp-wave ripples, independently of CA3
- Spike-local field potential coupling is weakest in the slow gamma band during ripples
- Optogenetically induced overlapping ripples also give rise to spurious gamma power
- Firing of superficial entorhinal cortex cells precedes longest sharp-wave ripples

Oliva et al., 2018, Cell Reports *25*, 1693–1700
November 13, 2018
https://doi.org/10.1016/j.celrep.2018.10.066

CellPress

Cell Reports
Report

Origin of Gamma Frequency Power during Hippocampal Sharp-Wave Ripples

Azahara Oliva,[1,3,5] Antonio Fernández-Ruiz,[1,5] Eliezyer Fermino de Oliveira,[1,4] and György Buzsáki[1,2,6,*]
[1]New York University Neuroscience Institute, New York, NY 10016, USA
[2]Center for Neural Science, New York University, New York, NY 10016, USA
[3]Department of Neuroscience, Zuckerman Mind Brain Behavior Institute, Columbia University, New York, NY 10027, USA
[4]Center for Mathematics, Computing and Cognition, Universidade Federal do ABC, São Bernardo do Campo, São Paulo, Brazil
[5]These authors contributed equally
[6]Lead Contact
*Correspondence: gyorgy.buzsaki@nyumc.org
https://doi.org/10.1016/j.celrep.2018.10.066

SUMMARY

Hippocampal sharp-wave ripples (SPW-Rs) support consolidation of recently acquired episodic memories and planning future actions by generating ordered neuronal sequences of previous or future experiences. SPW-Rs are characterized by several spectral components: a slow (5–15 Hz) sharp-wave, a high-frequency "ripple" oscillation (150–200 Hz), and a slow "gamma" oscillation (20–40 Hz). Using laminar hippocampal recordings and optogenetic manipulations, we dissected the origin of these spectral components. We show that increased power in the 20–40 Hz band does not reflect an entrainment of CA1 and CA3 neurons at gamma frequency but the power envelope of overlapping ripples. Spike-local field potential coupling between unit firing in CA1 and CA3 regions during SPW-Rs is lowest in the gamma band. Longer SPW-Rs are preceded by increased firing in the entorhinal cortex. Thus, fusion of SPW-Rs leads to lengthening of their duration associated with increased power in the slow gamma band without the presence of true oscillation.

INTRODUCTION

Hippocampal sharp-wave ripples (SPW-Rs) are one of the most synchronous spontaneous population patterns in the mammalian brain. They represent a complex event, composed of the sharp wave, a large-amplitude negative polarity deflection (40–-120 ms) in CA1 apical dendrites, and a short-lived fast oscillatory pattern (120–250 Hz) of the local field potential in the CA1 pyramidal layer, known as "ripples" (Buzsáki, 1986, 2015; Buzsáki et al., 1983, 1992; O'Keefe and Nadel, 1978; Suzuki and Smith, 1987). SPWs and ripples most often occur together, although they involve different physiological mechanisms. SPW-Rs serve as a mechanism to replay previous experiences for memory consolidation or plan future actions and influence decisions (Buzsáki, 2015; Foster, 2017).

SPW-Rs emerge when the brain is disengaged from the environment, most prominently during consummatory behaviors and non-rapid eye movement (REM) sleep (Buzsáki et al., 1983). Such brain state changes are associated with a decrease of subcortical neuromodulators and, consequently, the increasing efficacy of the excitatory interactions in the recurrent CA3 system (Buzsáki et al., 1983; Hasselmo and Sarter, 2011). More recent findings suggest that the population bursts underlying the SPW emerge in the CA2-CA3a recurrent collaterals and spread to the CA3b and CA3c regions (Oliva et al., 2016a). However, other factors, such as various network patterns in the neocortex, entorhinal cortex, and dentate gyrus, can also bias the exact occurrence and probability of SPW-Rs (Battaglia et al., 2004; Isomura et al., 2006; Headley et al., 2017; Sirota et al., 2003; Sullivan et al., 2011).

Recent reports described that SPW-Rs are phase-coupled with a power spectral peak in the slow gamma band (20–40 Hz). From this relationship, the authors assumed that ripple power is modulated by the phase of a genuine gamma oscillation and associated with a higher fidelity replay of past experiences and of place cell trajectories (Carr et al., 2012; Pfeiffer and Foster, 2015). The main source of slow gamma oscillation in the hippocampus is the CA3 region (Csicsvari et al., 2003; Fernández-Ruiz et al., 2012; Schomburg et al., 2014), which also entrains the CA1 region. However, it is not clear how the same CA1 circuit can be simultaneously engaged in both ripple and slow gamma oscillations. Alternatively, the slow gamma power increase, coincidental with SPW-Rs, may be a spurious oscillation because of the merging of adjacent ripples into longer events, resulting in an artificial increase of power in the gamma band. The present study provides support in favor of the latter alternative by demonstrating that slow gamma power is specifically associated with longer SPW-Rs produced by the overlap of multiple ripple events.

RESULTS

Spectral Components of SPW-Rs

SPW-Rs recorded in the CA1 pyramidal layer during waking quiescence are heterogeneous, ranging from short Gaussian-shaped events to longer irregular patterns (Figure 1A). Spectrogram of waking SPW-Rs (Figure 1B) revealed two slower-frequency components in addition to the well-characterized ripple oscillation (120–200 Hz). One of these slower components in the 2–15 Hz frequency band most likely corresponded to the

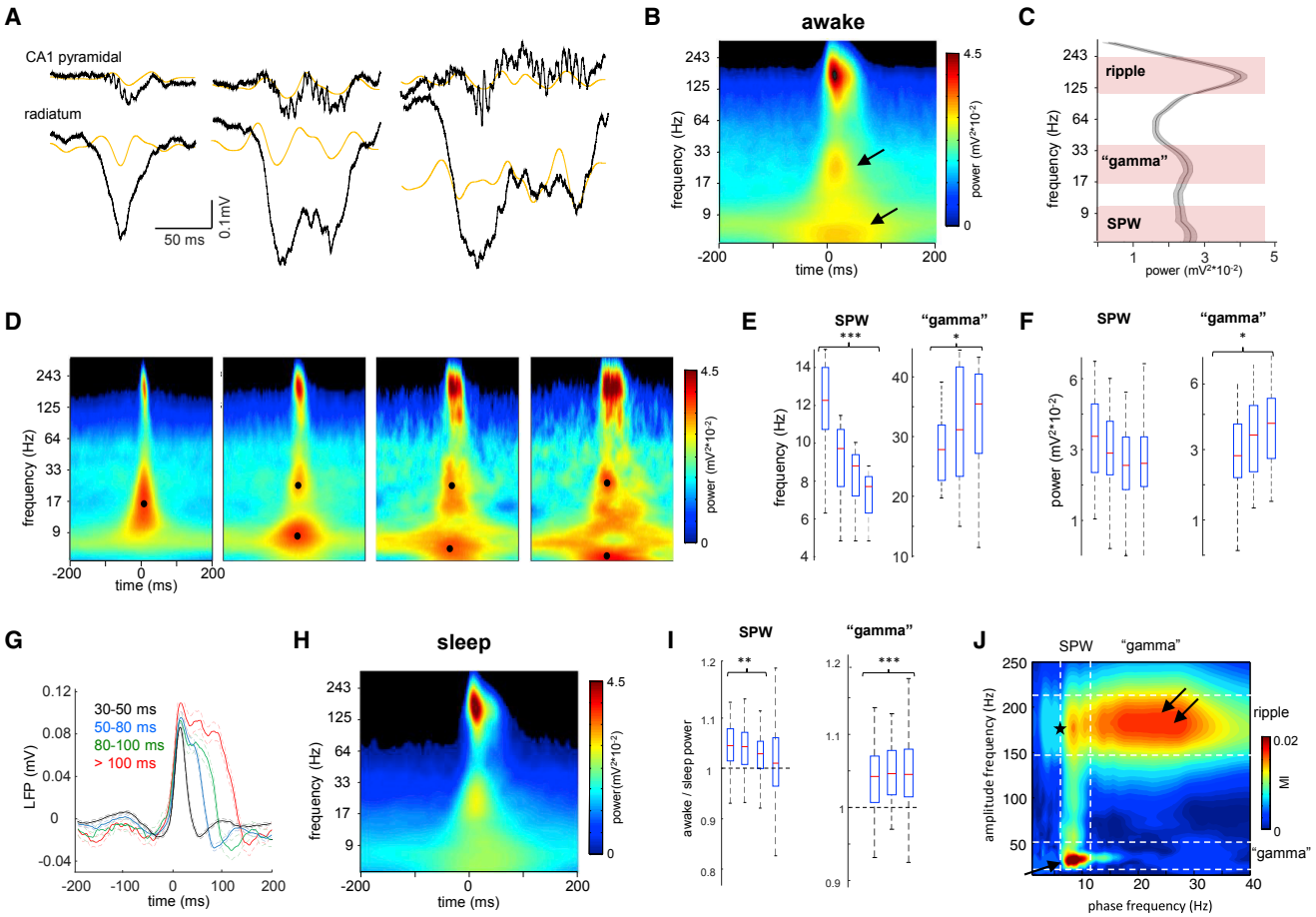

Figure 1. Nature of Different Spectral Components of SPW-R Complexes

(A) Examples of different length SWP-Rs. Wide-band (1 Hz to 20 kHz) LFP traces from the CA1 pyramidal layer and str. radiatum. Orange traces are 20–50 Hz filtered LFPs. Gray traces are power envelope in the 100–300 Hz band.

(B) Average peri-SPW-R wavelet spectrogram (n = 12 animals) during waking immobility. In addition to the ripple (~150 Hz), two other spectral components appear in lower-frequency bands, one around ~30 Hz and other below 10 Hz (arrows).

(C) Derivative of peri-SPW-R wavelet spectrogram at the SPW-R peak from 5 to 300 Hz identifies three spectral peaks: 120–250 Hz (ripple band), 17–40 Hz (gamma band), and 5–15 Hz (sharp-wave band).

(D) Average spectrograms of all SPW-R events detected during waking immobility (54 sessions in 12 rats) divided according to their durations: 30–50, 50–80, 80–100, and 100–300 ms. Note that spectrograms for the shorter events display only two frequency components, while for longer ones the slow frequency activity is segregated in two separate components. Black dots correspond to the maximal power in the "gamma" and SPW bands.

(E and F) Distribution of the (E) mean frequency and (F) power for the SPW and "gamma" bands for events of different duration. Shorter events only have SPW, no "gamma" component. *p < 0.05, ***p < 0.001, post hoc Tukey's test for all SPW-R events in the different duration categories.

(G) Wide-band peri-SPW-R pyramidal layer LFP averages for events of different duration. Note the presence of two or three "bumps" for longer events.

(H) Average peri-SPW-R wavelet spectrogram (n = 54 sessions in 12 animals) during non-REM sleep.

(I) Ratio of awake versus sleep power of SPW and gamma bands for events of different duration. **p < 0.01, ***p < 0.001, signed rank test.

(J) Averaged phase-amplitude comodulogram for CA1 pyramidal layer LFP revealed cross-frequency coupling between SPW phase and "gamma" (arrow) and ripple amplitudes (double arrow), and between "gamma" phase and ripple amplitude (star).

sharp wave. The other component was between 20 and 40 Hz (Figures 1B and 1C), in line with the report by Carr et al. (2012).

To understand the origin and mechanisms of these segregated frequency components, we separated SPW-Rs during awake immobility periods (n = 15,564 events in 12 rats) by duration and divided them into four groups: 30–50, 50–80, 80–100, and >100 ms. Wavelet spectrograms for these four groups revealed that the gamma frequency component appeared only in SPW-Rs longer than 50 ms in duration (Figure 1D). Note that previous studies discarded these short-duration SPW-Rs (Carr et al., 2012; Pfeiffer and Foster, 2015). The spectral peak of the 2–15 Hz component gradually decreased in frequency with SPW-R duration and corresponded to the median duration of the corresponding SPW-Rs (Figure 1E; $p < 0.001$; one-way ANOVA for all events of the four duration categories, followed by Tukey's post hoc test; linear correlation with $r = -0.78$, $p < 0.001$, Student's t). We suggest that it reflects the passive return currents in the pyramidal layer from the SPW sink in the CA1

stratum radiatum (Fernández-Ruiz et al., 2012; Sullivan et al., 2011). In agreement with this interpretation, the power of the 2–15 Hz component was larger in the stratum (str.) radiatum, where the CA3 to CA1 synapses are located (Figure S1). In contrast, the frequency and power of the "gamma" component increased with SPW-R duration (Figure 1F; $p < 0.05$ for frequency and power, Tukey's post hoc test; $r = 0.6/0.47$, $p < 0.001$, Student's t test), even though ripple frequency remained constant ($p > 0.05$, Tukey's post hoc test; $p > 0.05$, Student's t test). The relationship between the slow "gamma" and SPW-R duration led us to hypothesize that they are related. The wide-band peri-SPW-R local field potential (LFP) averages from the pyramidal layer offered support to this hypothesis (Figure 1G). Although shorter events typically had a smooth Gaussian shape (black trace; $p > 0.05$, Hartigan's dip test of unimodality followed by bootstrap for all events in the first two duration categories), longer events had several "bumps," whose duration corresponded to the 20–40 Hz band ($p < 0.01$, bootstrap). Inspection of the wide-band traces suggested that longer SPW-Rs were composed of multiple shorter events and that the observed slow gamma power in the peri-SPW-R spectrograms reflected LFP fluctuations due to the partially overlapping SPW-Rs. Analysis of the CA3 pyramidal layer LFP revealed the presence of a lower-frequency ripple compared with CA1 (117 ± 9 Hz; Oliva et al., 2016a) and an increase in low-frequency power around SPW-R occurrence, but not two distinct spectrally segregated components as in CA1 (Figure S1).

SPW-Rs during non-REM sleep share both similarities and differences with waking SPW-Rs (Figure 1H; Figure S1; $n = 54$ sessions in 12 animals). During sleep the frequency of ripple, "gamma," and SPW was similar to awake ($p > 0.05$, signed rank test), but the power of the gamma component was significantly lower (Figure 1I; Figure S1; $p < 0.001$, one-way ANOVA followed by Tukey's post hoc test), in agreement with previous observations (Carr et al., 2012).

To assess the interaction between all spectral components during SPW-Rs, we performed phase-amplitude cross-frequency coupling LFP analysis (Figure 1J). We found the strongest modulation between the phase of the SPW (5–10 Hz) and the amplitude of "gamma" (20–40 Hz; 0.020 ± 0.004 modulation index [MI]; $p < 0.001$, surrogate test; $n = 54$ sessions). In addition, ripple amplitude was phase-modulated by both the 2–10 Hz (0.011 ± 0.002 MI; $p < 0.001$, surrogate test) and gamma frequency band (0.0040 ± 0.001 MI; $p < 0.001$, surrogate test), suggesting that "gamma" phase-ripple amplitude coupling may be the consequence of the modulation of both "gamma" and ripple by SPW phase.

To test the hypothesis that the slow "gamma" component during SPW-Rs reflects concatenated SPW-Rs, we virally expressed ChR2 in CA1 pyramidal neurons and optogenetically induced concatenated synthetic "ripples" (Stark et al., 2014) using brief blue light pulses delivered through three optic fibers placed above the pyramidal layer (Figure 2A). These manipulations induced ripple-like oscillations in the pyramidal layer that had similar frequency and shape to spontaneously occurring SPW-Rs (Figures 2B and 2C; 153 ± 14 and 131 ± 11 Hz for spontaneous and induced ripples, respectively; $n = 10$ sessions in 4 rats). Induced ripples also elicited strong CA1 pyramidal cell and interneuron firing rate increases, similarly to spontaneous events (Figure S2). In contrast with spontaneous SPW-Rs that are typically accompanied by SPW current sinks in the CA1 str. radiatum, the optogenetically induced ripples were not associated with a str. radiatum sink (Figure 2D). Instead, ripples were superimposed on a negative LFP component in str. oriens and a corresponding positive wave in str. radiatum, implying that they were generated locally by the CA1 network, independent of the CA3 input (Figures 2B and 2D).

Wavelet spectrograms of optogenetically induced ripples revealed a strong power increase in the ripple band (120–200 Hz) but lacked the slow gamma component characteristic of some spontaneous events (Figure 2E). This result illustrates that slow gamma is not necessary for the local generation of ripples in CA1 and the two phenomena can be effectively decoupled. However, when we delivered two light pulses within a short time interval (any pulse interval between 5 and ~30 ms), we induced two partially overlapping ripples that were associated with a prominent gamma component in the wavelet spectrum. The frequency of the induced gamma component negatively correlated with the duration of ripple separation (Figure 2H; $r = -0.84$, $p < 0.01$, Student's t), whereas ripple frequency was not affected (Figure 2H; $p > 0.05$, Student's t test; $n = 10$ sessions in 4 rats). This gamma component faded when the separation between pulses was increased above ~30–50 ms and two separate ripple events were induced (Figures 2E and 2F; $p < 0.01$, rank sum test for <30 versus >50 ms pulse separation). To explicitly verify that the slow gamma component reflects the fusion of ripple events, we progressively increased the duration of the induced ripples by applying longer stimulation pulses (Figure S2). Single longer light pulses induced ripples of varying lengths, but not a distinct slow gamma component, in contrast with the overlapping ripple events (Figure S2; $p > 0.05$, rank sum test for single long pulses versus double pulses).

In a further demonstration of the spurious nature of gamma "oscillation" underlying SPW-Rs, we used simulated waveforms, mimicking the combination of SPW and ripple, and concatenated two such ripples with varying intervals. These simulations revealed that the gamma component can be induced when neighboring ripple events partially overlapped in time (Figures 3A and 3C), closely resembling the results of our optogenetic experiments. We repeated these simulations using only the slow envelopes of the concatenated ripples. Even though these waveforms lacked the high-frequency ripple component and consisted of only overlapping envelopes, gamma band power was similarly induced (Figures 3B and 3D). Similar to the optogenetic experiments, gamma frequency power negatively correlated with the inter-event separation (Figure 3D).

Single-Unit Responses during SPW-Rs of Different Durations

To examine further that the slow gamma band arises from concatenated SPW-Rs, we examined whether single units in the CA1 and CA3 regions were similarly modulated as the LFP events. Peri-SPW-R firing rate histograms for short events (<80 ms; black and blue curves in Figure 4) revealed a sharp, unimodal activation for both CA1 (Figure 4A; $n = 1,052$ pyramidal cells, $n = 171$ putative interneurons; $p > 0.05$, Hartigan's dip

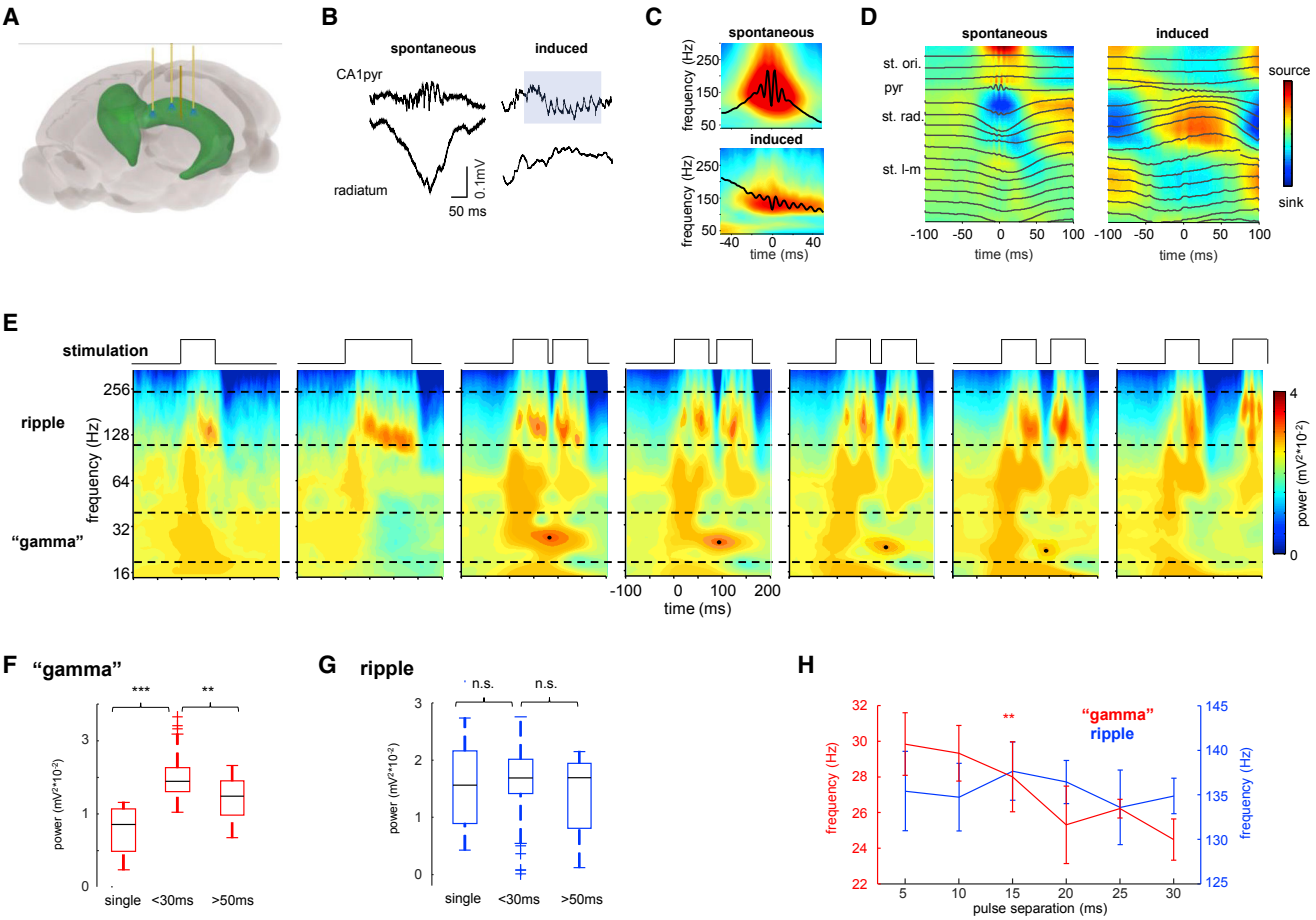

Figure 2. Spectral Features of Optogenetically Induced Ripples

(A) Schema of optogenetic experiments showing three optic fibers and one linear silicone probe implanted in dorsal CA1.

(B) Example of spontaneous and induced ripples from the same session. Note that spontaneous, but not optogenetically induced, ripples are accompanied by a sharp-wave in the CA1 stratum radiatum.

(C) Average wavelet spectrogram for spontaneous and induced ripples (n = 10 sessions in 4 animals).

(D) Example LFP (black traces) and CSD depth profiles for spontaneous and induced ripples in one session.

(E) Averaged wavelet spectrograms for an example rat, generated with different types of light pulses (black traces): single pulse 70-ms duration, single pulse 140-ms duration, two 70-ms pulses spaced 5, 10, 15, 20, and 70 ms. Black dots mark the largest power of the "gamma" component.

(F and G) Power in the (G) ripple and (F) "gamma" bands for single pulses and double pulses of separation <30 ms and >50 ms. ***$p < 0.001$, **$p < 0.01$, rank sum test.

(H) Frequency in the "gamma," but not in the ripple, band was correlated with pulse separation (**$p < 0.01$, Student's t).

pyr, pyramidal layer; st. l-m, stratum lacunosum-moleculare; st. ori., stratum oriens; st. rad., stratum radiatum.

test of unimodality followed by bootstrap; n = 54 sessions in 12 rats) and CA3 pyramidal cells and interneurons (Figure 4B; n = 646 pyramidal cells, n = 77 putative interneurons; $p > 0.05$, bootstrap). In contrast, both CA1 and CA3 neurons displayed several bumps at approximately slow gamma frequency during longer events (>80 ms; green and red curves in Figure 4; $p < 0.001$, bootstrap), resembling the shape of LFP envelope of SPW-Rs (compare with Figure 1G). These results suggest that longer waking SPW-Rs correspond to the concatenation of shorter events (Figure S3 shows non-REM data).

We also analyzed the strength of spike-LFP coupling during SPW-Rs. We performed a wide-band analysis by calculating wavelet phases from the CA1 pyramidal layer LFP at the times of spike occurrence from 5 to 300 Hz. This method enabled unbiased identification of frequency bands with preferred spike phase modulation (Fernández-Ruiz et al., 2017; Schomburg et al., 2014). As expected, discharges of both CA1 pyramidal cells and interneurons were strongly coupled to the SPW (2–10 Hz; 0.17 ± 0.02/0.15 ± 0.02 mean ± SEM modulation strength for pyramidal cells and interneurons) and ripple (110–240 Hz; 0.13 ± 0.01/0.06 ± 0.01 modulation strength) bands (Figure 4C). In contrast, coupling to the slow gamma band was weak (0.07 ± 0.01/0.04 ± 0.01 modulation strength; $p < 0.001/0.05$ for pyramidal cells and interneurons, one-way ANOVA followed by Tukey's post hoc test). Similar results were also observed for CA3 pyramidal cells and interneurons, although ripple frequency modulation

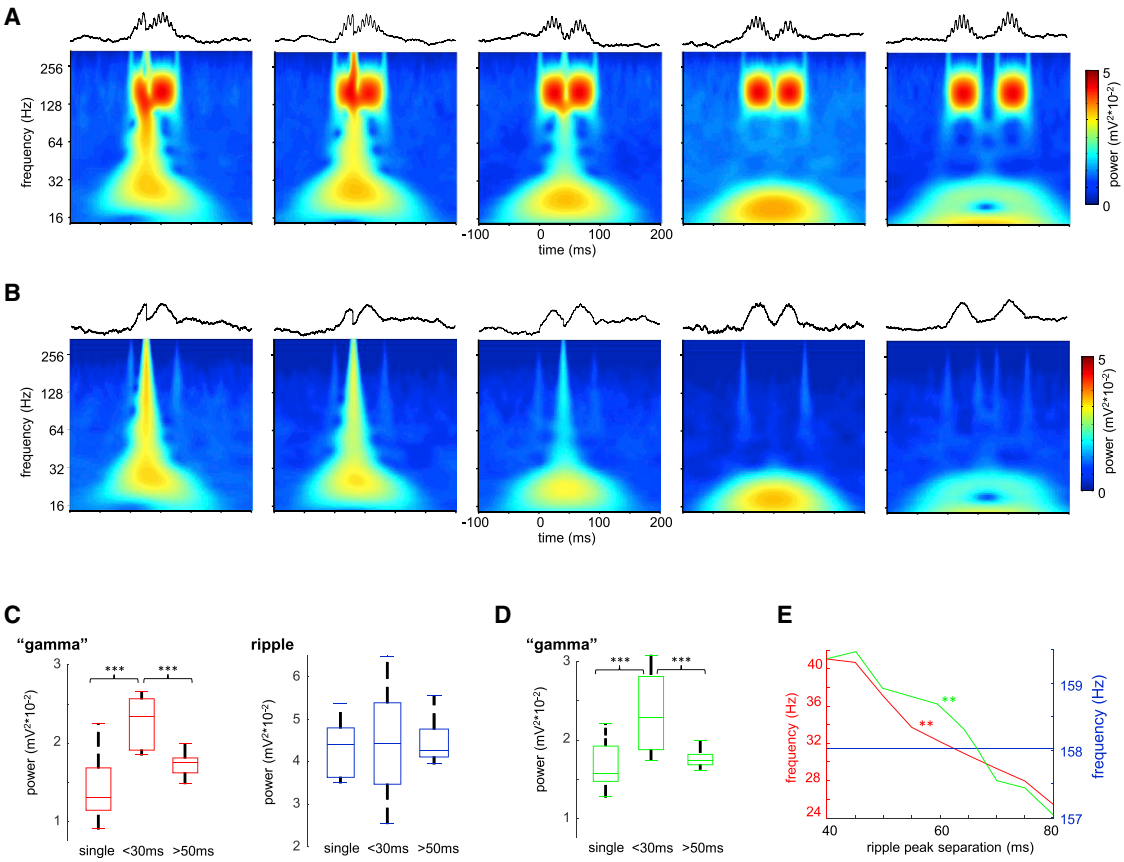

Figure 3. Synthetic Ripple Pairs Induce Slow Gamma Power

(A) Average wavelet spectrograms for synthetic ripple pairs with progressively longer inter-ripple interval. Note emerging "gamma" band with concatenated ripple doublets. Upper traces illustrate examples of simulated ripples.

(B) Same as in (A), but in this case similar events were simulated but without the high-frequency "ripple" component, i.e., only the slow envelope. Note that in this case similar slow gamma band power appeared.

(C) Power in the "gamma" and ripple bands for single pulses and double pulses of <30 and >50 ms separation. ***$p < 0.001$, rank sum test.

(D) Same as in (C) but for events without ripple component. ***$p < 0.001$, rank sum test.

(E) Frequency in the "gamma" (red and green curves for events with and without ripple oscillation respectively), but not in the ripple (blue), band was correlated with pulse separation (**$p < 0.01$, Student's t test).

in CA3 was largely absent (Figure 4D; 0.01 ± 0.001/0.01 ± 0.002 modulation strength; Buzsáki et al., 1983; Sullivan et al., 2011).

Finally, we examined the SPW-R modulation of unit firing in the main upstream region of the hippocampus, layers 2/3 of the entorhinal cortex (EC). EC excitatory (Figure 4E; n = 455 units in 37 sessions from 9 rats) and putative inhibitory (Figure S3; n = 111) units were activated by SPW-Rs, but their response was weaker and delayed compared with the CA1 and CA3 regions ($p < 0.001$ for peak firing rate time lags; Tukey's post hoc test). This likely reflects the multi-synaptic activation of EC layer 2/3 neurons in response to the CA1 drive (Chrobak and Buzsáki, 1996; Sullivan et al., 2011). Surprisingly, for the longest duration events, the main peak appeared at approximately 50 ms prior to CA1 SPW-R onset during waking state (arrow in Figure 4E; −55 ± 9 ms), but not during sleep. This suggests that entorhinal input can trigger SPW-Rs in the hippocampus during awake state and contribute to the longer-duration events. In further support of this hypothesis, neurons in layer 5 of the EC, the main target of the CA1 output, did not show this earlier peak but, instead, fired only after the CA1 SPW-R (Figure S3).

DISCUSSION

Employing laminar recordings, spanning all layers of dorsal CA1 and CA3, we identified three spectral components that compose SPW-R complexes: (a) a slow component, or sharp-wave (~5–15 Hz), elicited by a depolarizing volley from CA3 to CA1 apical dendrites and is most prominent in the str. radiatum (Fernández-Ruiz et al., 2012; Sullivan et al., 2011); (b) the second component is the ripple event (130–200 Hz) with the largest power in the CA1 pyramidal layer; and (c) a third component is the slow gamma band (~20–40 Hz). Both the frequency and power of the gamma component were correlated with SPW-R duration (Figure 1). The phase of the sharp-wave modulated both ripple and gamma amplitude, and the latter two were nested. Using optogenetic induction of CA1 ripples, we were able to decouple

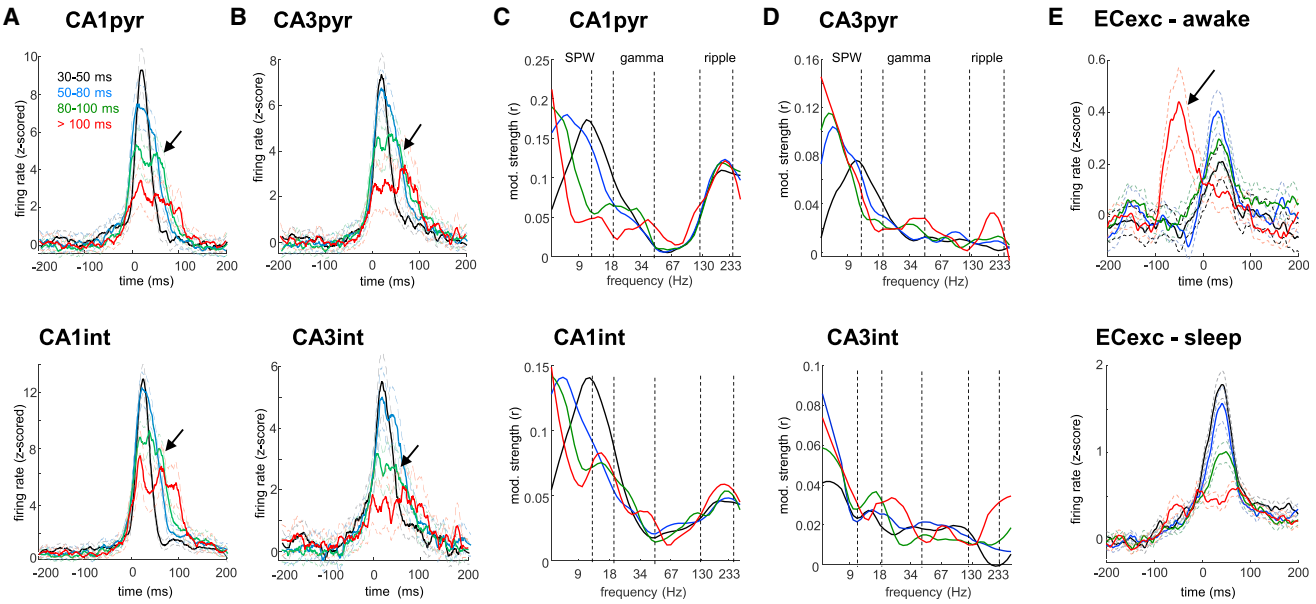

Figure 4. Single-Unit Response to SPW-Rs of Different Duration

(A) Discharge patterns of CA1 pyramidal cells (pyr) and interneurons (int) firing during awake SPW-Rs of different durations (black, blue, green, and red traces for progressively longer events). Note several "bumps" in the firing pattern of neurons during the longer-duration events (arrows).

(B) Same as in (A) but for CA3 pyramidal cells and interneurons.

(C and D) Distribution of the modulation strengths of (C) CA1 and (D) CA3 pyramidal cells and interneuron spikes by the CA1 pyramidal layer LFP phase in different frequency bands (5–300 Hz). Vertical dashed lines indicate boundaries of SPW, gamma, and ripple bands. Note that the unit-LFP modulation strength is lowest in the "gamma" band.

(E) Peri-SPW-R discharge patterns of entorhinal layer 2/3 excitatory cells (ECexc) during awake and sleep states. Note the additional firing rate peak prior to SPW-R onset appearing only for longest duration events during awake immobility (arrow).

ripples from the CA3 input (Figure 2). When a single ripple was induced, regardless of its duration, no "gamma" component was present. However, when two overlapping ripples with short peak intervals were induced, a gamma frequency component appeared in the spectrum and its frequency decreased with ripple separation. Similar results were obtained by simulation of overlapping ripple events. These results suggest that the slow gamma power observed during SPW-Rs is not a true oscillatory entrainment of CA3 and CA1 assemblies but rather reflects the fusion of two or more SPW-Rs.

Several potential mechanisms can generate longer-duration SPW-Rs. First, the CA3 recurrent circuit recruits a population discharge of variable duration (Traub and Wong, 1982). The second potential mechanism is that SPW bursts emerge stochastically at multiple CA3 locations and fuse together when traveling toward each other in the septo-temporal or fimbrio-subicular axis (Patel et al., 2013). These traveling events then can fuse together, resulting in longer SPW-Rs with variable diversity of neuronal content in CA1 (Figure S4). The third possibility is that an extrahippocampal input, such as the entorhinal input, leads to a prolongation of SPW-R events (Figure 4E). Each of these different mechanisms may give rise to gamma power in the 20–40 Hz band. Previous studies assumed that such increased gamma power reflects a true oscillation in the CA3 region, which in turn entrains both CA3 and CA1 circuits and phase-modulates ripple power in CA1 (Carr et al., 2012; Gillespie et al., 2016; Pfeiffer and Foster, 2015).

While phenomenologically the distinction between these options appears subtle (both can elicit SPW-R-associated gamma power), viewed from neuronal mechanisms, they are quite different. Our findings suggest that SPW-Rs do not require the presence of gamma oscillations. First, short-duration SPW-Rs were not associated with gamma power. Second, optogenetically induced single ripples did not generate slow gamma power either even when the duration of the optogenetic stimulation was prolonged (Figures 2 and S2). Third, entrainment of pyramidal cells and interneurons in the gamma band was the weakest of all frequencies in both CA3 and CA1 regions (Figure 3). In contrast, gamma oscillations in the absence of SPW-Rs during both theta and non-theta states occupy a higher frequency band (30–60 Hz) and strongly entrain neuronal populations within and across CA1 and CA3 regions (Colgin et al., 2009; Csicsvari et al., 2003; Fernández-Ruiz et al., 2017; Lasztóczi and Klausberger, 2017; Montgomery and Buzsáki, 2007; Schomburg et al., 2014). Lastly, only longer-duration SPW-Rs (>50 ms), naturally occurring or optogenetically induced, were associated with gamma power. However, power increase in the gamma band cannot be taken for evidence of the presence of an oscillation. Instead, we hypothesized that increased power in the gamma band is brought about by overlapping SPW-Rs.

Partially Overlapping SPW-Rs Induce Gamma Power

We observed that during longer SPW-Rs CA1 and CA3 pyramidal cells and interneurons fired in successive clusters,

concurrent with the LFP "bumps," instead of displaying a smooth unimodal rate increase as during short events (Figure 4). This observation suggested that slow gamma power during SPW-Rs occurs spuriously rather than physiologically, resulting from the overlap of two or more SPW-R events. Our observations that the lengthening duration of SPW-Rs and the increasing temporal offset of the bumps correlated with the decreasing frequency of slow gamma power supports this hypothesis (Figure 1). Furthermore, the weakest modulation of pyramidal neurons occurred in this LFP band.

To provide independent support for the concatenation hypothesis, we mimicked the physiological observations by optogenetic induction of ripples in the CA1 region, independent of its upstream inputs and by a computational model of SPW-Rs. By changing the intervals between the peaks of the individual events, we demonstrate that the slow gamma power can be induced by fusing successive ripple events (Figures 2 and 3). Overall, these findings are most compatible with the idea that SPW-Rs are a "quantal" phenomenon, i.e., occur in discrete packets (Pfeiffer and Foster, 2015), possibly aided by $GABA_B$-mediated hyperpolarization of pyramidal cells during the post-SPW-R period (English et al., 2014), and this process can generate prolonged events with power in the 20–40 Hz or clusters of successive SPW-R events. Because the individual SPW-Rs likely emerge from different CA3 subpopulations (Patel et al., 2013), the spike content of such overlapping SPW-Rs is a long unique event (Pfeiffer and Foster, 2015). Our results extend previous reports demonstrating that the features of ripple-band LFPs correlate with the spike content of SPW-Rs (Taxidis et al., 2015; Valero et al., 2017) and show that the wide-band LFP spectrum also carries information about the dynamics of CA1 and CA3 ensemble activation.

Entorhinal Input Contributes to Long-Duration SPW-Rs

Yamamoto and Tonegawa (2017) recently demonstrated that medial entorhinal input is necessary for the generation of ripple clusters and long-duration replay in CA1 neurons specifically during the awake state, even though replay in the EC and hippocampus can occur independently (O'Neill et al., 2017). Therefore, we examined whether the EC contributes to the long-duration SPW-Rs in our experiments. Both SPW-R-associated slow gamma power and multi-peaked activation of CA1 and CA3 cells were reduced during sleep (Figure S1). Importantly, we found that entorhinal layer 2/3 neurons were robustly active approximately 50 ms prior to the onset of longest CA1 SPW-Rs in the waking animal. In contrast, during non-REM sleep the firing probability of layer 2/3 entorhinal principal cells was inversely correlated with the duration of CA1 SPW-Rs (Figure 3). Overall, these findings establish that the entorhinal input plays a critical role in long-duration and clustered SPW-Rs, selectively in the waking brain, although it remains to be investigated whether the duration of SPW-R decreases with elapsed time after reward (Ólafsdóttir et al., 2016).

STAR★METHODS

Detailed methods are provided in the online version of this paper and include the following:

SUPPLEMENTAL INFORMATION

Supplemental Information includes four figures and can be found with this article online at https://doi.org/10.1016/j.celrep.2018.10.066.

ACKNOWLEDGMENTS

We thank Steven A. Siegelbaum and Antal Berényi for scientific support and advice; Dan English, Viktor Varga, Stephanie Rogers, Peter Petersen, Juan Ramirez-Villegas, Michel Besserve, and Manuel Valero for insightful comments. This work has been supported by EMBO Postdoctoral Fellowship ALTF 120-2017 (to A.O.), a Sir Henry Wellcome Postdoctoral Fellowship (to A.F.-R.), FAPESP grant 2017/03729-2 (to E.F.d.O.), and NIH grants NS034994, MH54671, and NS074015 (to G.B.).

AUTHOR CONTRIBUTIONS

A.O., A.F.-R., and G.B. conceived and designed the experiments; A.O., A.F.-R., and E.F.d.O. performed experiments and analyzed data; and A.O., A.F.-R., and G.B. wrote the manuscript with contributions from all authors.

DECLARATION OF INTERESTS

The authors declare no competing interests.

Received: March 9, 2018
Revised: August 7, 2018
Accepted: October 18, 2018
Published: November 13, 2018

REFERENCES

Battaglia, F.P., Sutherland, G.R., and McNaughton, B.L. (2004). Hippocampal sharp wave bursts coincide with neocortical "up-state" transitions. Learn. Mem. *11*, 697–704.

Buzsáki, G. (1986). Hippocampal sharp waves: their origin and significance. Brain Res. *398*, 242–252.

Buzsáki, G. (2015). Hippocampal sharp wave-ripple: a cognitive biomarker for episodic memory and planning. Hippocampus *25*, 1073–1188.

Buzsáki, G., Leung, L.W., and Vanderwolf, C.H. (1983). Cellular bases of hippocampal EEG in the behaving rat. Brain Res. *287*, 139–171.

Buzsáki, G., Horváth, Z., Urioste, R., Hetke, J., and Wise, K. (1992). High-frequency network oscillation in the hippocampus. Science *256*, 1025–1027.

Carr, M.F., Karlsson, M.P., and Frank, L.M. (2012). Transient slow gamma synchrony underlies hippocampal memory replay. Neuron *75*, 700–713.

Chrobak, J.J., and Buzsáki, G. (1996). High-frequency oscillations in the output networks of the hippocampal-entorhinal axis of the freely behaving rat. J. Neurosci. *16*, 3056–3066.

Colgin, L.L., Denninger, T., Fyhn, M., Hafting, T., Bonnevie, T., Jensen, O., Moser, M.B., and Moser, E.I. (2009). Frequency of gamma oscillations routes flow of information in the hippocampus. Nature *462*, 353–357.

Csicsvari, J., Jamieson, B., Wise, K.D., and Buzsáki, G. (2003). Mechanisms of gamma oscillations in the hippocampus of the behaving rat. Neuron *37*, 311–322.

English, D.F., Peyrache, A., Stark, E., Roux, L., Vallentin, D., Long, M.A., and Buzsáki, G. (2014). Excitation and inhibition compete to control spiking during hippocampal ripples: intracellular study in behaving mice. J. Neurosci. *34*, 16509–16517.

Fernández-Ruiz, A., and Herreras, O. (2013). Identifying the synaptic origin of ongoing neuronal oscillations through spatial discrimination of electric fields. Front. Comput. Neurosci. *7*, 5.

Fernández-Ruiz, A., Makarov, V.A., Benito, N., and Herreras, O. (2012). Schaffer-specific local field potentials reflect discrete excitatory events at gamma frequency that may fire postsynaptic hippocampal CA1 units. J. Neurosci. *32*, 5165–5176.

Fernández-Ruiz, A., Oliva, A., Nagy, G.A., Maurer, A.P., Berényi, A., and Buzsáki, G. (2017). Entorhinal-CA3 dual-input control of spike timing in the hippocampus by theta-gamma coupling. Neuron *93*, 1213–1226.e5.

Foster, D.J. (2017). Replay comes of age. Annu. Rev. Neurosci. *40*, 581–602.

Gillespie, A.K., Jones, E.A., Lin, Y.H., Karlsson, M.P., Kay, K., Yoon, S.Y., Tong, L.M., Nova, P., Carr, J.S., Frank, L.M., and Huang, Y. (2016). Apolipoprotein E4 causes age-dependent disruption of slow gamma oscillations during hippocampal sharp-wave ripples. Neuron *90*, 740–751.

Hartigan, J.A., and Hartigan, P.M. (1985). The dip test of unimodality. Ann. Stat. *13*, 70–84.

Hasselmo, M.E., and Sarter, M. (2011). Modes and models of forebrain cholinergic neuromodulation of cognition. Neuropsychopharmacology *36*, 52–73.

Headley, D.B., Kanta, V., and Paré, D. (2017). Intra- and interregional cortical interactions related to sharp-wave ripples and dentate spikes. J. Neurophysiol. *117*, 556–565.

Isomura, Y., Sirota, A., Ozen, S., Montgomery, S., Mizuseki, K., Henze, D.A., and Buzsáki, G. (2006). Integration and segregation of activity in entorhinal-hippocampal subregions by neocortical slow oscillations. Neuron *52*, 871–882.

Kadir, S.N., Goodman, D.F.M., and Harris, K.D. (2014). High-dimensional cluster analysis with the masked EM algorithm. Neural Comput. *26*, 2379–2394.

Lasztóczi, B., and Klausberger, T. (2017). Distinct gamma oscillations in the distal dendritic fields of the dentate gyrus and the CA1 area of mouse hippocampus. Brain Struct. Funct. *222*, 3355–3365.

Mizuseki, K., Sirota, A., Pastalkova, E., and Buzsáki, G. (2009). Theta oscillations provide temporal windows for local circuit computation in the entorhinal-hippocampal loop. Neuron *64*, 267–280.

Montgomery, S.M., and Buzsáki, G. (2007). Gamma oscillations dynamically couple hippocampal CA3 and CA1 regions during memory task performance. Proc. Natl. Acad. Sci. USA *104*, 14495–14500.

Montgomery, S.M., and Buzsáki, G. (2009). Behavior-dependent coordination of multiple theta dipoles in the hippocampus. J. Neurosci. *29*, 1381–1394.

O'Keefe, J., and Nadel, L. (1978). The Hippocampus as a Cognitive Map (Oxford University Press).

Ólafsdóttir, H.F., Carpenter, F., and Barry, C. (2016). Coordinated grid and place cell replay during rest. Nat. Neurosci. *19*, 792–794.

Oliva, A., Fernández-Ruiz, A., Buzsáki, G., and Berényi, A. (2016a). Role of hippocampal CA2 region in triggering sharp-wave ripples. Neuron *91*, 1342–1355.

Oliva, A., Fernández-Ruiz, A., Buzsáki, G., and Berényi, A. (2016b). Spatial coding and physiological properties of hippocampal neurons in the Cornu Ammonis subregions. Hippocampus *26*, 1593–1607.

O'Neill, J., Boccara, C.N., Stella, F., Schoenenberger, P., and Csicsvari, J. (2017). Superficial layers of the medial entorhinal cortex replay independently of the hippocampus. Science *355*, 184–188.

Patel, J., Schomoburg, E.W., Berényi, A., Fujisawa, S., and Buzsáki, G. (2013). Local generation and propagation of ripples along the septotemporal axis of the hippocampus. J Neurosci. *33*, 17029–17041.

Pfeiffer, B.E., and Foster, D.J. (2015). PLACE CELLS. Autoassociative dynamics in the generation of sequences of hippocampal place cells. Science *349*, 180–183.

Rossant, C., Kadir, S.N., Goodman, D.F., Schulman, J., Hunter, M.L., Saleem, A.B., Grosmark, A., Belluscio, M., Denfield, G.H., Ecker, A.S., et al. (2016). Spike sorting for large, dense electrode arrays. Nat Neurosci. *19*, 634–641.

Schomburg, E.W., Fernández-Ruiz, A., Mizuseki, K., Berényi, A., Anastassiou, C.A., Koch, C., and Buzsáki, G. (2014). Theta phase segregation of input-specific gamma patterns in entorhinal-hippocampal networks. Neuron *84*, 470–485.

Sirota, A., Csicsvari, J., Buhl, D., and Buzsáki, G. (2003). Communication between neocortex and hippocampus during sleep in rodents. Proc. Natl. Acad. Sci. USA *100*, 2065–2069.

Stark, E., Roux, L., Eichler, R., Senzai, Y., Royer, S., and Buzsáki, G. (2014). Pyramidal cell-interneuron interactions underlie hippocampal ripple oscillations. Neuron *83*, 467–480.

Sullivan, D., Csicsvari, J., Mizuseki, K., Montgomery, S., Diba, K., and Buzsáki, G. (2011). Relationships between hippocampal sharp waves, ripples, and fast gamma oscillation: influence of dentate and entorhinal cortical activity. J. Neurosci. *31*, 8605–8616.

Suzuki, S.S., and Smith, G.K. (1987). Spontaneous EEG spikes in the normal hippocampus. I. Behavioral correlates, laminar profiles and bilateral synchrony. Electroencephalogr. Clin. Neurophysiol. *67*, 348–359.

Taxidis, J., Anastassiou, C.A., Diba, K., and Koch, C. (2015). Local field potentials encode place cell ensemble activation during hippocampal sharp wave ripples. Neuron *87*, 590–604.

Traub, R.D., and Wong, R.K. (1982). Cellular mechanism of neuronal synchronization in epilepsy. Science *216*, 745–747.

Valero, M., Averkin, R.G., Fernandez-Lamo, I., Aguilar, J., Lopez-Pigozzi, D., Brotons-Mas, J.R., Cid, E., Tamas, G., and Menendez de la Prida, L. (2017). Mechanisms for selective single-cell reactivation during offline sharp-wave ripples and their distortion by fast ripples. Neuron *94*, 1234–1247.e7.

Yamamoto, J., and Tonegawa, S. (2017). Direct medial entorhinal cortex input to hippocampal CA1 is crucial for extended quiet awake replay. Neuron *96*, 217–227.e4.

Ylinen, A., Bragin, A., Nádasdy, Z., Jandó, G., Szabó, I., Sik, A., and Buzsáki, G. (1995). Sharp wave-associated high-frequency oscillation (200 Hz) in the intact hippocampus: network and intracellular mechanisms. J. Neurosci. *15*, 30–46.

STAR★METHODS

KEY RESOURCES TABLE

REAGENT or RESOURCE	SOURCE	IDENTIFIER
Antibodies		
GFP tag monoclonal antibody	Thermo Fisher	Cat #: A-11120; RRID AB_221568
Goat anti-mouse secondary antibody Alexa Fluor 488	Thermo Fisher	Cat #: A-11001; RRID AB_2534069
Bacterial and Virus Strains		
AAV5-CaMKIIa-hChR2(H134R)-EYFP	UNC Vector Core	N/A
Chemicals, Peptides, and Recombinant Proteins		
DAPI	Sigma-Aldrich	Cat#: D8417
Deposited Data		
Hippocampus – entorhinal electrophysiological data	crcns.org (hc-3 dataset)	https://doi.org/10.12688/f1000research.3895.2
Hippocampal data from novel environment sessions	crcns.org (hc-11 dataset)	https://doi.org/10.6080/K0862DC5
Experimental Models: Organisms/Strains		
Rat: Long-Evans	Charles River	Cat#: Crl:LE 006
Software and Algorithms		
MATLAB	Mathworks	N/A
KlustaViewa	Rossant et al., 2016	https://github.com/klusta-team/klustaviewa/
Spikedetekt2	Cortical Processing Laboratory (UCL)	https://github.com/klusta-team/spikedetekt2
KlustaKwik2 Kadir et al., 2014 https://github.com/klusta-team/klustakwik/	KlustaKwik2 Kadir et al., 2014 https://github.com/klusta-team/klustakwik/	KlustaKwik2 Kadir et al., 2014 https://github.com/klusta-team/klustakwik/
FMA toolbox Michael Zugaro http://fmatoolbox.sourceforge.net/	FMA toolbox Michael Zugaro http://fmatoolbox.sourceforge.net/	FMA toolbox Michael Zugaro http://fmatoolbox.sourceforge.net/
Circular Statistics Toolbox Philipp Berens https://www.mathworks.com/matlabcentral/fileexchange/10676-circular-statistics-toolbox-directional-statistics	Circular Statistics Toolbox Philipp Berens https://www.mathworks.com/matlabcentral/fileexchange/10676-circular-statistics-toolbox-directional-statistics	Circular Statistics Toolbox Philipp Berens https://www.mathworks.com/matlabcentral/fileexchange/10676-circular-statistics-toolbox-directional-statistics
Wavelet analysis toolbox	C Torrence and GP Compo	http://atoc.colorado.edu/research/wavelets/
Custom-made analysis tools	https://github.com/buzsakilab/buzcode	N/A

CONTACT FOR REAGENT AND RESOURCE SHARING

Further information and requests for resources and datasets should be directed to and will be fulfilled by the Lead Contact, György Buzsáki (gyorgy.buzsaki@nyumc.org). All data will be available at CRCNS.org after publication.

EXPERIMENTAL MODEL AND SUBJECT DETAILS

A total of 17 adult male Long-Evans rats (300-450 g, 3-6 months old) were used in this study. Most of these animals were used in previous studies and detailed description and experimental procedures can be found there (Oliva et al., 2016a, 2016b; Fernández-Ruiz et al., 2017; Mizuseki et al., 2009). Four new animals were operated and recorded for this study, as detailed below. Rats were kept in the vivarium on a 12-hour light/ dark cycle and were housed 2-3 per cage before surgery and individually after it. All experiments were approved by the Institutional Animal Care and Use Committee at New York University Medical Center.

METHOD DETAILS

Surgical Procedures

Animals were anesthetized with isoflurane anesthesia and craniotomies were performed under stereotaxic guidance. Different types of silicon probes (NeuroNexus, Ann-Arbor) were implanted in the dorsal hippocampus and in some cases (n = 9), also in the entorhinal cortex. High-density silicon probes were mounted on custom-made micro-drives to allow their precise vertical movement after implantation. The probes were inserted above the target region and the micro-drives were attached to the skull with dental cement. The craniotomies were sealed with sterile wax. Two stainless steel screws were drilled bilaterally over the cerebellum served as ground and reference for the recordings. Several additional screws were driven into the skull and covered with dental cement to strengthen the implant. Finally, a copper mesh was attached to the skull with dental cement and connected to the ground screw to act as a Faraday cage, attenuating the contamination of the recordings by environmental electric noise. After post-surgery recovery, the probes were moved gradually in 75 to 150 μm steps per day until the desired position was reached. The pyramidal layer in the CA1, 2 and 3 regions was identified physiologically by increased unit activity and characteristic LFP patterns (Ylinen et al., 1995; Oliva et al., 2016a; 2016b). The identification of dendritic sublayers in CA1, DG and CA3 was achieved by the application of CSD and ICA analysis to the LFPs (Fernández-Ruiz et al., 2012; Fernández-Ruiz and Herreras, 2013) and by known physiological markers such as ripples (140-200 Hz), reversal of sharp-waves (Ylinen et al., 1995) and depth versus amplitude profile of theta oscillations (Buzsáki, 1986; Montgomery and Buzsáki, 2009).

Optogenetic Experiments

For optogenetic experiments, rats were injected with AAV5-CaMKIIa-hChR2(H134R)-EYFP from UNC Vector Core (a gift from Dr. Karl Deisseroth). Three injections of 150 nL each were performed along the longitudinal axis of the dorsal hippocampi, right above the CA1 pyramidal layer. After injection, craniotomies were sealed and animals recovered in the vivarium for three weeks. Following this period, a new surgical procedure for implanting optic fibers and electrodes was performed. 200 μm core optic fibers (Thor Labs) were implanted in the same craniotomies used previously for virus injection, right above CA1 pyramidal layer. Optic fibers were directly coupled to 460 nm blue light-emitting laser diodes (PL-450, Osram; Stark et al., 2014). A silicon probe was implanted in a different craniotomy, targeting also the dorsal CA1 region.

To induce ripple generation in CA1 brief pulses (35 to 210 ms) were delivered simultaneously through all fibers. The intensity was manually adjusted in each animal by gradually increasing light power until a high-frequency oscillation was evoked. To minimize broad-band artifacts at the onset of the stimulation, trapezoid pulses with a 20 ms ramp were used. Pulses were delivered every 5 s while the rat rested in its home cage.

Behavioral Recordings

After surgery, animals where handled daily and accommodated to the recording room and cables for 1 to 3 weeks before the start of the experiments. Prior to the start of the experiment animals were water restricted. 30 - 60-minute-long behavior sessions were conducted daily, preceded and followed by 1-3 hours sleep sessions. Data from multiple navigational tasks was pooled for the analyses, including running on a linear (190 or 240 cm long with 10-20 cm walls) or circular track (100 cm diameter) for water reward and exploration in an enclosed open field (120 cm square, 30 cm walls) or open circular platform (120 cm diameter 'cheesboard maze') for small food pellets. In the linear tracks animals received water rewards (~0.2 mL) in both ends each time they traveled from one end to the other. All animals spontaneously performed this behavior and typically continue doing so until they were satiated, then session ended. On the circular maze rats were made to run in a clockwise direction by preventing the counter-clockwise movement until the rats' behavior became stereotyped (~10 minutes). Water reward was delivered in a predetermined 30 cm reward area only when the animals had performed a full clockwise run. In the open field and circular platform animals explored to collect cereal crumbles that were randomly throwed by the experimenter. All animals spontaneously adopt this behavior and sessions lasted until they were not longer running. All rooms had different prominent distal cues around the maze, clearly visible for the animals. 2-4 hours' sleep sessions always followed exploration sessions. Animal position was monitored using video tracking of two LEDs mounted on the head-stage.

Tissue Processing and Immunohistochemistry

Following the termination of the experiments, animals were deeply anesthetized and perfused transcardially first with 0.9% saline solution followed by 4% paraformaldehyde solution. Brains were sectioned in 50-70 μm thick slices (Leica Vibratome) parallel with the plane of the implanted electrodes.

For virus injected animals, immunohistochemistry was performed to verify the expression of the conjugated YFP-ChR2 construct. Slices were washed three times PBS (0.1 M), followed by 2 additional 20 minutes' washes in TBS-T (Triton 0.3%), then blocked with 10% bovine serum albumin in TBS-T for 45 minutes. After that, slices were incubated for 1 hour at room temperature followed by 48 hours at 4°C with the primary antibody solution containing mouse anti-GFP (1:500, Invitrogen A-11120) in TBS-T. After three washes in TBS, sections were incubated for 2h at room temperature with goat anti-mouse Alexa Fluor 488 (1:300, Invitrogen A-11001). Sections were finally washed and mounted on glass slides with fluorescence medium (Fluoroshield with DAPI - F6057, Sigma, USA).

QUANTIFICATION AND STATISTICAL ANALYSIS

Spike Sorting and Unit Classification

Neuronal spikes were detected from the digitally high-pass filtered LFP (0.5–5 kHz) by a threshold crossing-based algorithm (*Spikedetekt2*). Detected spikes were automatically sorted using the masked EM algorithm for Gaussians mixtures implemented in *KlustaKwik2*, followed by manual adjustment of the clusters using *KlustaViewa* software to obtain well-isolated single units. Multiunit or noise clusters were discarded. Putative pyramidal cells and interneurons were separated on the basis of their autocorrelograms and waveform characteristics (Stark et al., 2014; Fernández-Ruiz et al., 2017), assisted by monosynaptic excitatory and inhibitory interactions between simultaneously recorded, well-isolated units (Mizuseki et al., 2009).

SPW-R Detection

Only non-theta states were studied. Theta epochs were detected automatically using the ratio of the power in theta band (5- 11 Hz) to the power of nearby bands (1-4 Hz, 12-14 Hz) of CA1 pyramidal layer LFP, followed by manual adjustment with the aid of visual inspection of whitened power spectra. Low theta power and low speed (less than 2 cm/s) epochs during wakefulness were classified as quiet wakefulness (referred as awake state through the text) and during sleep as non-REM sleep.

To detect ripples, the wide-band signal was band-pass filtered (difference-of-Gaussians; zero-lag, linear phase FIR), and instantaneous power was computed by clipping at 4 SD, rectified and low-pass filtered (Oliva et al., 2016a). The low-pass filter cut-off was at a frequency corresponding to π cycles of the mean band-pass (for 80-250 Hz band-pass, the low-pass was 55 Hz). The mean and SD of baseline LFP were computed based on the power during non-REM sleep. Subsequently, the power of the non-clipped signal was computed, and all events exceeding 4 SD from the mean were detected. Events were then expanded until the (non-clipped) power fell below 2 SD; short events (< 20 ms) were discarded. Sharp-waves were additionally also detected; LFP from str. radiatum channels was filtered with band-pass filter boundaries (5-40 Hz). LFP events of a minimum duration of 20 ms and maximum 400 ms exceeding 2.5 SD of the background signal were included as candidate SPWs. Only if a SPW was simultaneously detected with a ripple, a CA1 SPW-R event was retained for further analysis. SPW-R bursts were classified when more than one event was detected in a 400 ms time window.

Ripple Modulation of Unit Firing

Well-isolated putative units with at least 100 spikes in a given session were included in the analysis. For all individual units, spikes in a [-200, +200] ms peri-ripple peak window were collected and firing rate histograms (1 ms time bin) were constructed. All histograms for the same type of units (same region and cell type, i.e., pyramidal or interneuron) were pooled to construct population response histograms for each session (day). The firing rate histograms were z-scored and smoothed using a Gaussian kernel (SD = 5 ms). The significance of unit firing modulation by SPW-Rs was assessed performing surrogate tests (n = 1000 samples). Finally, data across sessions and animals was pooled to calculate grand-averages (across all sessions and animals).

Spectral Analysis, Cross-Frequency Coupling and Spike-LFP Coupling

To analyze high-frequency oscillatory activity in the LFP at a high resolution in time and frequency, the complex wavelet transform (CWT) of the LFP was calculated using complex Morlet wavelets (MATLAB, The MathWorks, Natick, MA). Wavelet spectrograms were calculated for each detected SPW-R in a [-200, +200] ms window and for the LFP in the center of the pyramidal layer. Spectrograms for individual events were averaged to construct final plots.

The phase-amplitude cross-frequency coupling during SPW-Rs was assessed using a modulation index (MI). Wavelet phase was calculated at 79 levels from 1-40 Hz, and the amplitude at 236 levels from 15-300 Hz. Phase time-series were binned into phase intervals and the mean wavelet amplitude was calculated for each of them. The MI was obtained by measuring the divergence of the observed amplitude distribution from the uniform distribution. The statistical significance of the MI values (p value) was assessed by a surrogate analysis (n = 1000 surrogates) with random shifts between the phase and amplitude time series (Schomburg et al., 2014).

The phase-locking of spikes to LFP features at each frequency was measured for individual units using the wavelet phase from 5-300 Hz (50 logarithmically spaced wavelet scales) at the time of each spike. Modulation indices were calculated using the mean resultant length of the phases, and significance was estimated using the Rayleigh test for non-uniformity.

All LFP analysis were performed with custom-made MATLAB scripts (The MathWorks, Natick, MA).

SPW-R Simulations

Simulated data consisted in pink noise mixed with synthetic SPW-Rs. SPW-Rs were generated as a sinusoid with amplitude A and frequency f_c following a normal distribution $N(\mu, \sigma)$ with $\mu = 140$ and $\sigma = 12$ Hz, and lasting for a fixed duration of 70 ms. The obtained sinusoid is then modulated by $m(t) = A_m sin(2\pi f_m t)$, where $A_m = 1$ and $f_m = 1/2t_{rip}$, being t_{rip} the ripple interval. Amplitude was defined as $A = \sigma_p 10^{(SNR/20)}$, where SNR is the signal-to-noise ratio, set at -20 dB, and the σ_p is the pink noise standard deviation. For simulations of sinusoid "envelopes" without ripple component, A was set to 0.

Statistical Analyses

All statistical analyses were performed with standard MATLAB functions or custom-made scripts. No specific analysis to estimate minimal population sample or group size was used, but the number of animals, sessions, recorded cells and SPW-R events were larger or similar to those employed in previous related works (e.g., Carr et al., 2012; Pfeiffer and Foster, 2015; Fernández-Ruiz et al., 2017; Gillespie et al., 2016; Oliva et al., 2016a). The unit of analysis was typically sessions, for example, when comparing spontaneous and induced SPW-R LFP features or convoluted unit response. In some cases, the unit of analysis was SPW-R events, for example when comparing spectral characteristics of events with different duration, and that is stated through the text. Unless otherwise noted, for all tests, non-parametric two-tailed Wilcoxon rank-sum (equivalent to Mann-Whitney U-test), Wilcoxon signed-rank or Kruskal-Wallis one-way analysis of variance were used. For multiple comparisons, Tukey's honesty post hoc test was employed, and the p values reported are always the lower of the post hoc multiple comparisons tests. To assess unimodality of a distribution, Hartigan's dip test was used (Hartigan and Hartigan, 1985) and its significance assessed by bootstrap (n = 1000). Due to experimental design constraints, the experimenter was never blind to the manipulation performed during the experiment (i.e., optogenetic manipulation).

DATA AND SOFTWARE AVAILABILITY

Part of the dataset included in this study is available in the CRCNS database (Hippocampus – entorhinal electrophysiological data: http://crcns.org [hc-3 dataset], https://doi.org/10.12688/f1000research.3895.2; Hippocampal data from novel environment sessions: http://crcns.org [hc-11 dataset], https://doi.org/10.6080/K0862DC5). The rest is currently under preparation to be deposited in the same database but will be immediately available upon request.

Custom MATLAB scripts can be downloaded from https://github.com/buzsakilab/buzcode.